PHYSICAL REVIEW B **90**, 214417 (2014)

Thermodynamic properties, electron spin resonance, and underlying spin model in $Cu_3Y(SeO_3)_2O_2Cl$

K. V. Zakharov,[1] E. A. Zvereva,[1] P. S. Berdonosov,[2] E. S. Kuznetsova,[2] V. A. Dolgikh,[2] L. Clark,[3] C. Black,[3] P. Lightfoot,[3] W. Kockelmann,[4] Z. V. Pchelkina,[5,6] S. V. Streltsov,[5,6] O. S. Volkova,[1,6] and A. N. Vasiliev[1,6,7,*]

[1]*Low Temperature and Superconductivity Department, Faculty of Physics,*
M.V. Lomonosov Moscow State University, Moscow 119991, Russia
[2]*Inorganic Chemistry Department, Faculty of Chemistry, M.V. Lomonosov Moscow State University, Moscow 119991, Russia*
[3]*School of Chemistry, University of St Andrews, St Andrews, Fife KY16 9ST, United Kingdom*
[4]*ISIS Facility, Rutherford Appleton Laboratory, Didcot, Oxfordshire OX11 0QX, United Kingdom*
[5]*Institute of Metal Physics, Russian Academy of Sciences, Ekaterinburg 620219, Russia*
[6]*Theoretical Physics and Applied Mathematics Department, Institute of Physics and Technology,*
Ural Federal University, Ekaterinburg 620002, Russia
[7]*National University of Science and Technology "MISiS", Moscow 119049, Russia*

(Received 28 May 2014; revised manuscript received 7 November 2014; published 5 December 2014)

We report a detailed study of the magnetic properties of the buckled kagome compound $Cu_3Y(SeO_3)_2O_2Cl$ using heat capacity, magnetization, powder neutron diffraction, electron spin resonance, and first-principles calculations. The crystal structure is confirmed to be isotypic with the mineral francisite, with orthorhombic space group symmetry *Pmmn* throughout the temperature range 5–300 K. Magnetization, heat capacity, and neutron diffraction confirm long range magnetic order below $T_N = 35$ K. The electron spin resonance spectra reveal the presence of two modes corresponding to two different crystallographic Cu positions. The principal g values of the g tensor of Cu1 sites were found to be $g_1 = 2.18(4)$, $g_2 = 2.10(6)$, and $g_3 = 2.05(9)$, while the effective g factor of Cu2 sites is almost isotropic and is on average $g = 2.09(5)$. At low temperatures, $Cu_3Y(SeO_3)_2O_2Cl$ undergoes a metamagnetic transition, with a critical field $B_C = 2.6$ T at 2 K, due to the suppression of the interplane exchange interactions and saturates in modest magnetic field $B_S \leqslant 8$ T. The first-principles calculations allow an estimation of both intraplane and interplane exchange interactions. The weakness of the interplane exchange interaction results in low values of the critical fields for the metamagnetic transition, while the competition between intraplane exchange interactions of different signs results in a similarly low value of the saturation field.

DOI: 10.1103/PhysRevB.90.214417 PACS number(s): 75.30.Cr, 75.30.Et, 75.47.Lx, 76.30.−v

I. INTRODUCTION

The diversity of crystal structures and the peculiar magnetic topologies found in minerals have attracted increasing attention of condensed matter physicists interested in quantum cooperative phenomena at low temperatures [1–5]. Among the recently discussed hot topics in this field are the pressure-induced superconductivity in calaverite $AuTe_2$ [6,7] and the formation of the gapped (or gapless) quantum spin liquid ground state in Herbertsmithite $ZnCu_3(OH)_6Cl_2$ [8–11].

The title compound $Cu_3Y(SeO_3)_2O_2Cl$ is a synthetic analog of the mineral francisite $Cu_3Bi(SeO_3)_2O_2Cl$, which crystallizes in the orthorhombic space group *Pmmn* with cell dimensions $a = 6.354(1)$ Å, $b = 9.630(1)$ Å, $c = 7.220(2)$ Å, and $Z = 2$ [12]. It consists of two-dimensional buckled kagome sheets of Cu^{2+} cations in the ab plane, containing eight-coordinated Bi^{3+}, square-planar (or tetragonally distorted octahedra) Cu^{2+}, and three-coordinated Se^{4+}. The chloride ions and the selenium lone pair electrons occupy tunnels parallel to [001], as shown in Fig. 1. Studies of the physical properties of francisite are limited to measurements of anisotropic thermal expansion, interpreted in terms of oxocentered copper-bismuth tetrahedra [13] and investigations of magnetism and optical birefringence in its synthetic analogs $Cu_3Bi(SeO_3)_2O_2X$ (X = Cl, Br, I) [14]. At low temperatures, long-range magnetic order was established in both Cl-based and Br-based compounds. The variation of the halogens in these phases results in a regular increase of unit cell parameters and elongation of the corresponding bonds. Hence, the magnetic properties of the bismuth oxohalides are very similar, with Néel temperatures of 24.2 and 23.8 K in the oxychloride and oxybromide, respectively [13].

Subsequent studies have concentrated on $Cu_3Bi(SeO_3)_2O_2Br$. Anisotropic magnetic properties in this compound have been studied by bulk magnetization measurements as well as powder and single-crystal neutron diffraction [15]. At $T_N = 27.4$ K the system develops an alternating antiferromagnetic order of the kagome layers, which individually exhibit a canted ferrimagnetic moment shown in Fig. 2, resulting from competing ferro- and antiferromagnetic intralayer exchange interactions. A magnetic field $B_C \sim 0.8$ T applied along the c axis triggers a metamagnetic transition, where every second layer flips resulting in a ferrimagnetic structure. Significantly higher fields are required to rotate the ferromagnetic component towards the b axis (~7 T) or towards the a axis (~15 T). Terahertz transmission spectra have been measured as a function of temperature and magnetic field on single crystals of $Cu_3Bi(SeO_3)_2O_2Br$ [16]. In time-domain spectra in the absence of an applied magnetic field, two resonance absorptions were observed below T_N. The corresponding resonance frequencies increase with decreasing temperature reaching energies of 1.28 and 1.23 meV. Multifrequency

---

[*] vasil@mig.phys.msu.ru

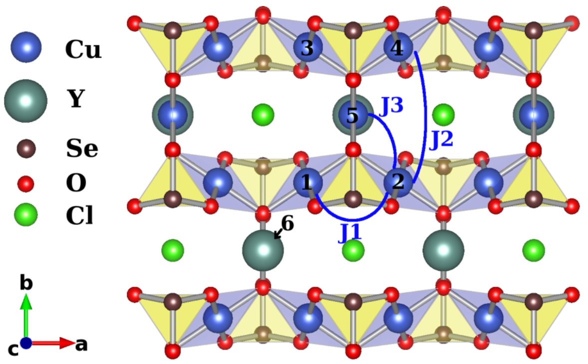

FIG. 1. (Color online) Structure of $Cu_3Y(SeO_3)_2O_2Cl$ in a mixed ball-and-stick and polyhedral representation. Large, medium, and small circles between corrugated copper-selenium planes represent yttrium, copper, and chlorine ions, respectively. The arcs indicate the main intraplane exchange interaction pathways.

electron spin resonance transmission spectra as a function of the applied magnetic field show the field dependence of four magnetic resonance modes, which were modeled as a ferromagnetic resonance.

Chemical substitutions can have a significant impact on the crystal structure and ensuing physical properties. For example, the replacement of selenium by tellurium induces a substantial transformation of the parent structure. In $Cu_3Bi(TeO_3)_2O_2Cl$, this results in the change of one of the copper coordinations from a CuO_4 square plane to a CuO_4Cl square pyramid. This leads to a doubled *c* parameter and a change in the space group to *Pcmn* [17]. On the other hand, the original *Pmmn* structure was reported for the erbium analog of francisite $Cu_3Er(SeO_3)_2O_2Cl$ [18] and no substantial variations in orthorhombic crystal structure were found for the series of lanthanide oxohalides $Cu_3Ln(SeO_3)_2O_2X$ (Ln = La, Nd, Sm, Eu, Gd, Dy, Ho, Er, Yb, Y; X = Cl, Br). The oxochlorides were formed with all lanthanides, while oxobromides were formed for Ln = La–Gd only [19].

In this present work we report a detailed study of the magnetic properties of $Cu_3Y(SeO_3)_2O_2Cl$ with heat capacity, magnetization, neutron diffraction, and electron spin resonance (ESR) studies, supported by first-principles calculations to determine the underlying spin model. This provides an important comparison to the previously well studied analog $Cu_3Bi(SeO_3)_2O_2Br$, which displays a unique noncollinear magnetic structure as a result of its interesting layered and magnetically frustrated topology. Instead of exhibiting the standard "spin-flop–spin-flip" succession of phase transitions, $Cu_3Bi(SeO_3)_2O_2Br$ undergoes a metamagnetic transition, as discussed above. It is important to determine whether this spectacular metamagnetic response is a general feature of the francisite family. To eliminate the complications of an additional magnetic sublattice due to a rare earth cation the yttrium-substituted compound was chosen.

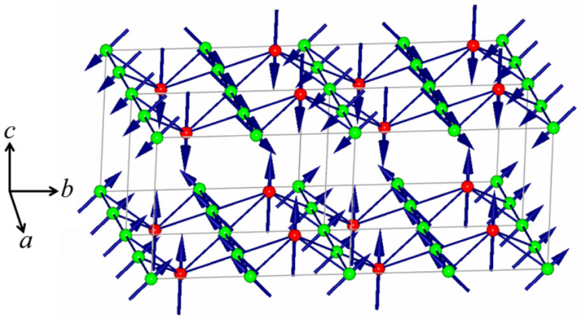

FIG. 2. (Color online) The spin model for $Cu_3L(SeO_3)_2O_2X$ (L = Bi, Y, X = Br, Cl) with Cu1 (green) moments canted from the *c* axis towards the *b* axis coupled ferromagnetically to the moments on the Cu2 (red) sites which aligned parallel to the *c* axis. The buckled kagome layers of Cu1 and Cu2 site cations are antiferromagnetically arranged with respect to one another. Note that the figure only shows one half of the magnetic unit cell along the *c* axis.

II. EXPERIMENT

$Cu_3Y(SeO_3)_2O_2Cl$ was prepared from a stoichiometric mixture of high purity Y_2O_3, CuO, $CuCl_2$, and SeO_2. The selenium dioxide was obtained from selenous acid, which was dehydrated under dynamic vacuum at a moderate temperature and then sublimed in a flowing mixture of dry air and NO_2 prepared by thermal decomposition of $Pb(NO_3)_2$. All preparatory procedures with SeO_2 were carried out in a dry box purged with argon. The stoichiometric reactant mixture was thoroughly ground in an agate mortar and transferred into quartz tube which was sealed under vacuum and placed into an annealing furnace with controlled heating. The mixture was heated to 300 °C over 12 h and kept at this temperature for 24 h. Then the temperature was raised to 575 °C over 12 h and maintained at this temperature for 72 h. This produced a green-colored powder product. Preliminary characterization used powder x-ray diffraction collected on a STOE Stadi P diffractometer equipped with a Ge (111) monochromator (Cu $K\alpha$ radiation, 2θ range 10°–115°), which confirmed phase purity according to the previously suggested structural model [19].

Magnetization and susceptibility data were taken on a Quantum Design Physical Property Measurement System (PPMS) over the temperature range 2–300 K in applied field strengths up to 9 T. Heat capacity was measured on a 10 mg sample of $Cu_3Y(SeO_3)_2O_2Cl$ in the same PPMS instrument using the relaxation method in the temperature range 2–300 K. Powder neutron diffraction data were collected for $Cu_3Y(SeO_3)_2O_2Cl$ on the GEM diffractometer at the ISIS spallation neutron source, Rutherford Appleton Laboratory. A 5.18 g powder sample was loaded into an 8 mm outer diameter vanadium can such that the sample covered the 400 mm height of the neutron beam. The sample was placed into a ^{4}He cryostat and diffraction data were taken over the temperature range 5–280 K. Rietveld analysis of the data was performed using the GSAS software [20]. ESR studies were carried out using an *X*-band ESR spectrometer CMS 8400 (ADANI) ($f \approx 9.4$ GHz, $B \leqslant 0.7$ T) equipped with a low temperature mount, operating in the range $T = 5$–300 K. The effective *g* factor has been calculated with respect to a BDPA (*a*,*g*-bisdiphenyline-*b*-phenylallyl) reference sample with $g_{\mathrm{et}} = 2.00359$. The first-principles calculations were performed on the Uran cluster of the IMM Ural Branch of RAS.

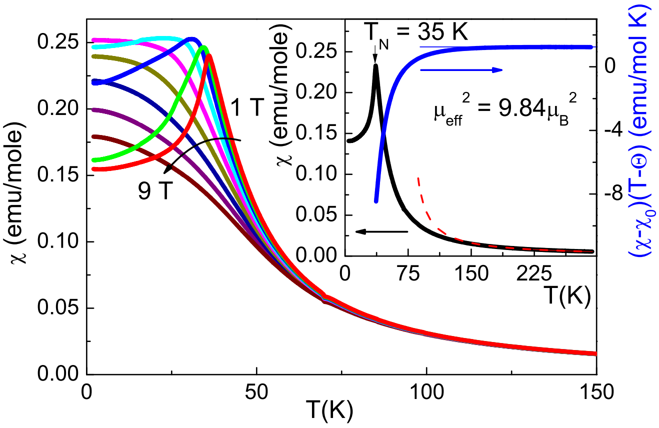

FIG. 3. (Color online) The temperature dependence of the magnetic susceptibility of $Cu_3Y(SeO_3)_2O_2Cl$ in applied field strengths of 1–9 T, with a field step of 1 T. The inset represents the temperature dependence of the magnetic susceptibility at 0.1 T along with the Curie constant as a function of temperature. The dotted line represents an extrapolation of the Curie-Weiss type dependence from the high temperature region.

III. RESULTS AND DISCUSSION

Figure 3 shows the temperature dependence of the magnetic susceptibility of $Cu_3Y(SeO_3)_2O_2Cl$ measured in various applied magnetic fields up to 9 T. At lower fields, the susceptibility data show a sharp peak characteristic of antiferromagnetic order at a Néel temperature $T_N = 36.3$ K. The inset to Fig. 3 shows the magnetic susceptibility measured in a 0.1 T field, which exhibits a one third drop for temperatures $T < T_N$ consistent with an easy-axis antiferromagnet. An increase in the applied magnetic field strength results in a broadening of the pronounced ordering transition and an apparent shift to higher temperatures. Eventually, the nature of the magnetic susceptibility becomes ferromagnetic for applied fields $B > 4$ T. The temperature dependence of the susceptibility can be modeled in terms of Curie-Weiss behavior with $\Theta = 75$ K and $C = 1.23$ emu/mol and a temperature independent term $\chi_0 = -1.56\times10^{-4}$ emu/mol. The positive sign of the Weiss constant Θ indicates the predominance of ferromagnetic exchange at elevated temperatures and the Curie constant C yields an effective magnetic moment $\mu_{\text{eff}}^2 = 9.84\mu_B^2$ per mole formula unit, which corresponds to a moment of $1.81\mu_B$ per Cu^{2+} cation. The value of χ_0 is the summation of individual ions Pascal's constants [21] and van Vleck magnetism of Cu^{2+} [22]. The inset of Fig. 3 also shows the temperature dependence of the Curie constant, which clearly shows the strengthening of antiferromagnetic interactions upon cooling. The magnetization of $Cu_3Y(SeO_3)_2O_2Cl$ as a function of field is shown in Fig. 4 measured over the temperature range 5–30 K. At low temperatures, the primary linear response changes into a sharp upturn at moderate magnetic fields and with increasing temperature this anomaly shifts to lower magnetic fields. The magnetization at 2 K and its field derivative are shown in the inset to Fig. 4. The metamagnetic transition at this temperature occurs at a critical field $B_C = 2.6$ T and at high fields the magnetization tends towards a slightly reduced saturated value than the expected $M_{\text{sat}} = ngS\mu_B = 3.165\mu_B$ per formula unit of three Cu^{2+} cations with $g = 2.11$. Further evidence for the appearance of long range order in $Cu_3Y(SeO_3)_2O_2Cl$ is given by the heat capacity C_p. The temperature dependence of C_p measured in various magnetic fields in the range 0–5 T are shown in Fig. 5. In the absence of a nonmagnetic analog for $Cu_3Y(SeO_3)_2O_2Cl$ it is difficult to separate the different contributions to the heat capacity. The modest magnitude of the peak at $T_N = 36.3$ K allows one to assume that a significant amount of magnetic entropy (S_{mag}) is released well above the transition temperature. Indeed, calculating the entropy released at the transition by subtracting off the high field specific heat as a rough estimation of the lattice contribution gives a value of $S_{\text{mag}} \sim 1.35\ \text{J mol}^{-1}\ \text{K}^{-1}$, which is to be compared with the thermodynamic value of $3R\ln 2 = 17.3\ \text{J mol}^{-1}\ \text{K}^{-1}$ (where R is the universal gas constant). Evidently the magnetic entropy released above the transition temperature constitutes more than 90% of the overall

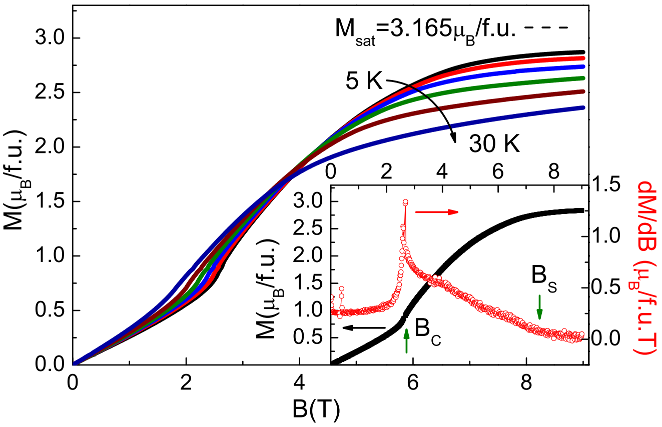

FIG. 4. (Color online) The field dependence of the magnetization in $Cu_3Y(SeO_3)_2O_2Cl$ over the temperature range of 5–30 K in steps of 5 K. The inset shows the field dependence of the magnetization at 2 K and its field derivative.

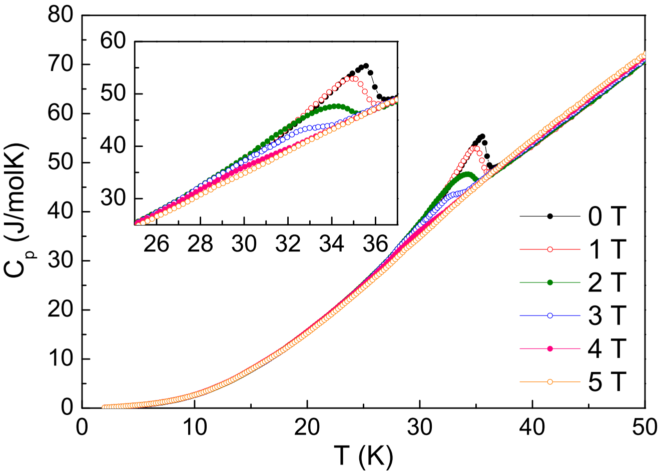

FIG. 5. (Color online) The temperature dependence of the heat capacity of $Cu_3Y(SeO_3)_2O_2Cl$ measured in zero field and applied field strengths of up to 5 T. The inset shows the field dependence of the heat capacity around the magnetic ordering transition in clearer detail.

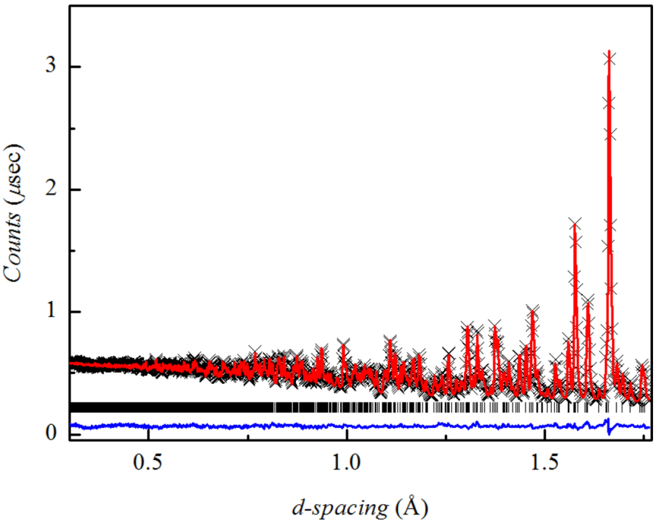

FIG. 6. (Color online) Plot of the Rietveld refinement of the *Pmmn* model to powder neutron diffraction data collected for $Cu_3Y(SeO_3)_2O_2Cl$ on the high resolution backscattering bank at 280 K.

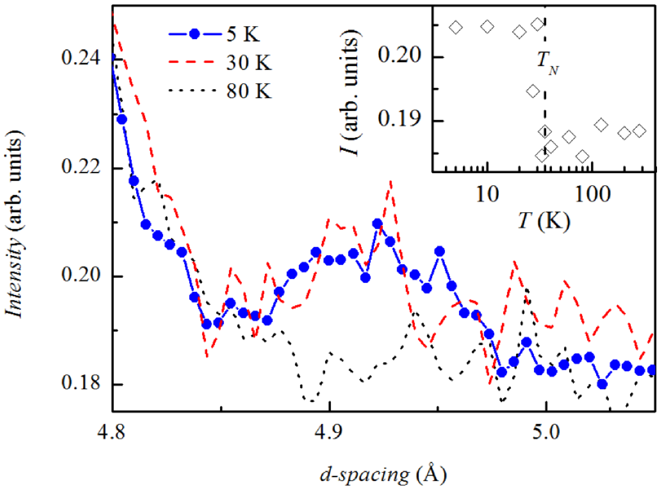

FIG. 7. (Color online) The neutron diffraction data of $Cu_3Y(SeO_3)_2O_2Cl$ at various temperatures showing the growth of the most distinct magnetic Bragg peak upon cooling below T_N. The inset shows the intensity of this magnetic reflection as a function of temperature.

magnetic entropy. This fact is in full agreement with the strong deviation of the experimental $\chi(T)$ data from the extrapolation of the high temperature Curie-Weiss law from below ~150 K, as shown in the inset to Fig. 3.

Figure 6 shows the Rietveld refinement of the orthorhombic *Pmmn* model to powder neutron diffraction data of $Cu_3Y(SeO_3)_2O_2Cl$ collected on the high resolution backscattering bank of the GEM diffractometer at 280 K. Lattice parameters, atomic positions, isotropic thermal parameters, background terms, diffractometer constants, wavelength-dependent absorption correction, scaling, and profile parameters refined simultaneously to four histograms (banks 3–6) to give an overall $R_{wp} = 2.15\%$ and $\chi^2 = 3.66$ for 81 variables. Table I gives a summary for the results of the *Pmmn* model. Upon cooling, the powder neutron diffraction data confirm the occurrence of the magnetic phase transition observed in the magnetic susceptibility, magnetization, and heat capacity data at $T_N = 36.3$ K through the appearance of magnetic Bragg peaks. The main magnetic reflections are present at d spacings of 4.5 and 4.9 Å and can be indexed by the magnetic propagation vector $\boldsymbol{k} = (0, 0, 0.5)$. Figure 7 shows the growth of the (1 1 0.5) reflection of the magnetic unit cell, the form of which as a function of temperature (see Fig. 7, inset) is indicative of a second-order magnetic phase transition. In order to calculate the potential symmetry-allowed magnetic structures that can result from such a phase transition representational analysis of the crystal structure with the $\boldsymbol{k}$ vector was performed using the 2 K version of the SARA*h*-representational analysis program [23]. SARA*h* determines the space group symmetry elements that leave the $\boldsymbol{k}$-vector invariant, which form the little group $G_{\boldsymbol{k}}$ and gives the representation of a crystallographic site in terms of the irreducible representations (IRs) of $G_{\boldsymbol{k}}$. For $Cu_3Y(SeO_3)_2O_2Cl$ with *Pmmn* space group symmetry and $\boldsymbol{k} = (0, 0, 0.5)$ there are eight symmetry elements that leave the $\boldsymbol{k}$ vector unchanged and the resulting IRs and their associated basis vectors (BVs) ψ_n are given in Table S1 of the Supplemental Material [24].

TABLE I. Refined atomic coordinates and isotropic thermal parameters within the *Pmmn* nuclear structural model for $Cu_3Y(SeO_3)_2O_2Cl$ at 280 K [$a = 6.2991(1)$ Å, $b = 9.4411(1)$ Å, $c = 6.9724(1)$ Å].

Atom	Site	*x*	*y*	*z*	Occ.	$U_{\text{iso}}/\text{Å}^2$
Y	2*a*	1/4	1/4	0.2660(1)	1.0	0.0059(3)
Cu1	4*c*	0	0	0	1.0	0.0081(2)
Cu2	2*a*	1/4	1/4	0.7955(2)	1.0	0.0081
Se	4*e*	1/4	0.5605(1)	0.5899(1)	1.0	0.0041(2)
Cl	2*b*	1/4	3/4	0.1465(1)	1.0	0.0222(3)
O1	4*e*	1/4	0.1103(1)	0.9969(1)	1.0	0.0044(2)
O2	8*g*	0.0397(1)	0.5881(1)	0.7373(1)	1.0	0.0079(2)
O3	4*e*	1/4	0.1193(1)	0.5748(1)	1.0	0.0074(3)

From powder diffraction data alone, it was difficult to obtain an unambiguous magnetic structure solution. However, an earlier single crystal neutron diffraction study [15] of the related material $Cu_3Bi(SeO_3)_2O_2Br$, which adopts the same *Pmmn* structure with the buckled kagome network of Cu^{2+} ions and undergoes a magnetic ordering transition at $T_N = 27.4$ K with the same $\boldsymbol{k}$-vector (0, 0, 0.5), revealed that the best fit to data was obtained for the magnetic structure given by the Γ_3 IR for both copper sites. Given the similarity of the two structures and the nature of the ordering transition, the Γ_3 model was selected as a magnetic model for the low temperature neutron diffraction data of $Cu_3Y(SeO_3)_2O_2Cl$. The magnetic Rietveld refinement was performed in GSAS using the SARA*h*-refine [23] program to set up the magnetic phase. The lattice parameters, isotropic thermal parameters, and profile parameters of the magnetic phase were constrained by the nuclear phase and once again, the nuclear and magnetic models were refined simultaneously to histograms collected on banks 3–6. Figure 8 shows the refinement to the small-angle (bank 3) data, where the magnetic reflections are most

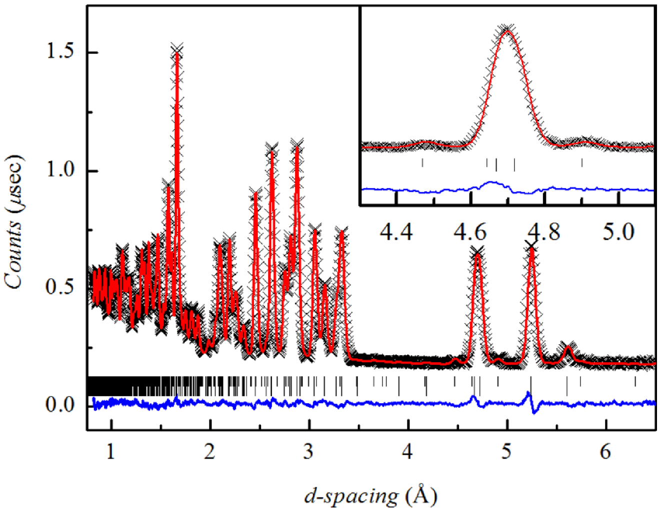

FIG. 8. (Color online) Rietveld refinement of the *Pmmn* nuclear model (bottom tick marks) and the Γ_3 magnetic model (top tick marks) to the small angle GEM diffraction data of $Cu_3Y(SeO_3)_2O_2Cl$ collected at 5 K. The inset shows the fit to the two main magnetic reflections.

apparent. The inset shows the fit to the data over the d-spacing range around the two main magnetic Bragg peaks, which demonstrates the excellent agreement between the Γ_3 model and the data. The refined magnetic moments were (0, 0.11(1), 0.40(2)) μ_B and (0, 0, 1.04(4)) μ_B for the Cu1 and Cu2 sites, respectively. An overall $R_{wp} = 2.15\%$ was achieved with a $\chi^2 = 4.28$ for 83 variables. The Γ_3 magnetic structure is shown in Fig. 2, with layers of Cu1 moments canted in the *ac* plane arranged ferromagnetically with the Cu2 moments which are oriented along the *c* axis. These layers couple antiferromagnetically with one another, which gives rise to the bulk antiferromagnetic behavior observed in our low field magnetic study.

We have also attempted to estimate the magnetic exchange parameters of the spin model of $Cu_3Y(SeO_3)_2O_2Cl$ through first-principles calculations. There are six Cu^{2+} cations in the unit cell, four on the Cu1 site labeled 1–4 and two on the Cu2 labeled 5 and 6 (see Fig. 1). There are three main magnetic exchange pathways within the buckled kagome layers of $Cu_3Y(SeO_3)_2O_2Cl$ which are denoted J_1 (between Cu1 ions along the a axis), J_2 (between Cu1 ions along the b axis), and J_3 (between Cu1 and Cu2 ions) and are shown in Fig. 1. These exchange parameters were calculated by mapping the Heisenberg model to the total energy difference of four magnetic configurations. The following magnetic structures were used: ferromagnetic (FM) FM (uuuuuu), FM_ch (uudduu), antiferromagnetic (AFM) AFM1 (uuuudd), and AFM2 (udduuu), where “u” and “d” denotes spin-up and spin-down orientations on the corresponding copper site (e.g., in the FM_ch configuration the first, second, fifth, and sixth Cu ions have a spin-up orientation, while the third and fourth are spin-down). The electronic structure calculations for these configurations were performed with the pseudopotential Quantum ESPRESSO code [25]. The exchange correlation potential was used in the form proposed by Perdew-Burke-Ernzerhof [26] with a wave function cutoff of 40 Ry. The GGA+U approximation was used to take the strong Coulomb interaction between the Cu sites into account. The Hund’s rule exchange and Coulomb repulsion were chosen to be $J_H = 0.9$ eV and $U = 7$ eV, respectively [27,28]. The unit cell of $Cu_3Y(SeO_3)_2O_2Cl$ contains only one layer of CuO_4 plaquettes. The lowest total energy in this case corresponds to a ferromagnetic state with an energy gap of 0.6 eV. Such a ferromagnetic configuration within one layer corresponds well with the spin model used to fit the low temperature powder neutron diffraction data discussed above and shown in Fig. 2. The total and partial densities of states obtained in the GGA+U calculation for the FM configuration are shown in Fig. 9. The top of the valence band and the bottom of the conduction band are formed by $3d$ states of copper, which are strongly hybridized with oxygen $2p$ states. The Cu^{2+} ions have a d^9 configuration with the one hole in the $3d$ shell, which is clearly seen in the spin resolved density of states for Cu1 and Cu2 ions. The electron density distribution corresponding to the one hole on a Cu^{2+} ion obtained in the GGA+U calculation is shown in Fig. 10. This orbital has $x^2 - y^2$ symmetry for both copper sites, and is directed towards the oxide ions within the plaquettes. The spin moments on Cu were found to be 0.6 μ_B, the slight reduction from the expected values is due to hybridization effects.

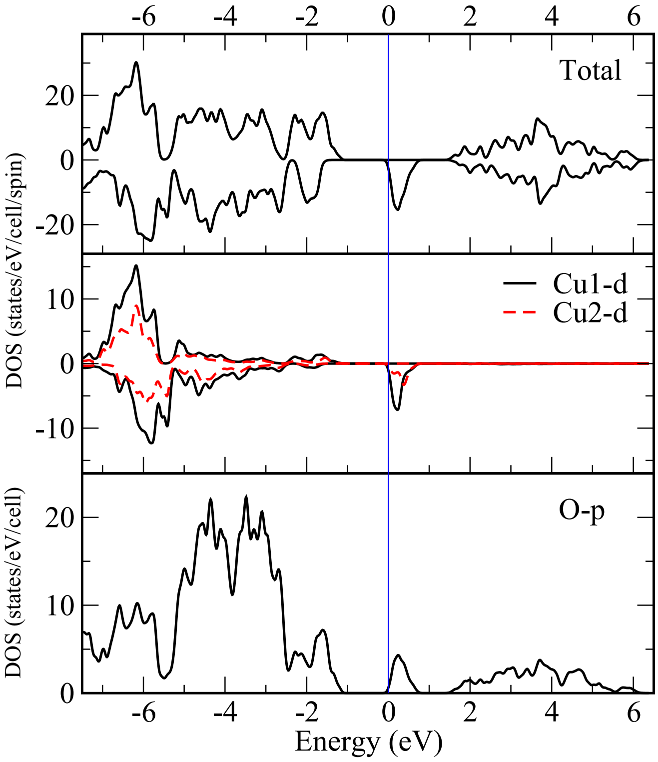

FIG. 9. (Color online) The total and partial density of states as calculated in the GGA+U approximation for the ferromagnetic (FM) configuration.

The calculated values of the exchange parameters are given by $J_1 = 137$ K (FM), $J_2 = -43$ K (AFM), and $J_3 = 78$ K (FM), respectively. The Curie-Weiss temperature recalculated from these exchange constants as $S(S+1)J(0)/3$ equals 129 K [where $J(0)$ is the sum of all neighboring exchange interaction

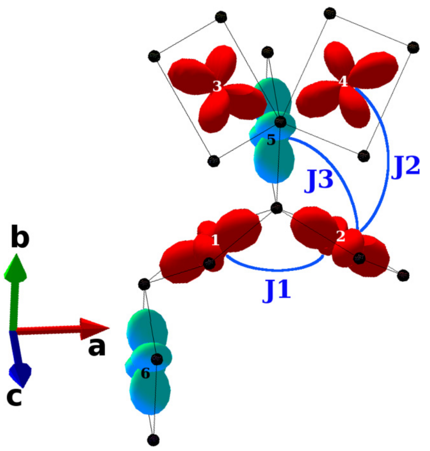

FIG. 10. (Color online) The electron density distribution around each Cu^{2+} cation as determined by the GGA+U calculation. The red and blue orbitals correspond to Cu1 and Cu2, respectively. Oxide ions are shown as black spheres.

parameters]. This reasonably agrees with the corresponding value extracted from the fit to the high temperature magnetic susceptibility data, since the mean-field approximation typically overestimates the Curie-Weiss temperature 1.5–2 times. The signs of exchange constants also agree with those estimated from the single crystal magnetic susceptibility measurements on the related compound $Cu_3Bi(SeO_3)_2O_2Br$ [15]. In contrast to Ref. [15], however, which assumes that $J_1 \sim J_3$, we have found here that J_1 and J_3 are quite different. This difference cannot be explained in terms of a superexchange mechanism since the Cu-O-Cu angles for the J_1 and J_3 exchange pathways are nearly the same (111.9° and 112.7°). One of the possible explanations for such a behavior could be the influence of the Se atoms that connect two of the Cu(1)O_4 plaquettes only. The hybridization with Se $4p$ orbitals may effectively change the proportion between FM and AFM contributions to the total exchange coupling as it was proposed for $CuGeO_3$ [29].

More generally, it is not obvious that such a complex magnetic system can be well described by a simple Heisenberg model. In order to check this, we calculated the total energy of an additional magnetic configuration, AFM3 (uuuuud), and recalculated the exchange parameters using the FM_ch, AFM, AFM2, and AFM3 magnetic structures (excluding the FM configuration). The values of exchange parameters obtained are identical to the ones presented above, which indicates the validity of the application of the Heisenberg model for the description of magnetic properties of $Cu_3Y(SeO_3)_2O_2Cl$. Since the exchange couplings are known to depend on the values of the Hubbard U parameter [30] the value of U was varied within a limit of 1 eV and the corresponding changes in J were within 7% of the original exchange parameter.

There are three possible interlayer exchange pathways connecting the buckled kagome layers: J_{c1} (between Cu1 and Cu1), J_{c12} (between Cu1 and Cu2), and J_{c2} (between Cu2 and Cu2). In order to estimate the interlayer exchange energy the unit cell was doubled along the c axis. The total energy of the seven different magnetic configurations was calculated within the GGA+U approximation. The lowest total energy was obtained for the spin configuration in which the ferromagnetic layers are stacked antiferromagnetically with respect to one another along the c direction, in agreement with the spin model obtained from the magnetic Rietveld refinement to low temperature neutron diffraction data discussed above. The resulting exchange integrals are given by $J_1 = 136$ K (FM), $J_2 = -42$ K (AFM), $J_3 = 85$ K (FM), $J_{c1} = 1.5$ K (FM), $J_{c12} = -8$ K (AFM), and $J_{c2} = 0.9$ K (FM).

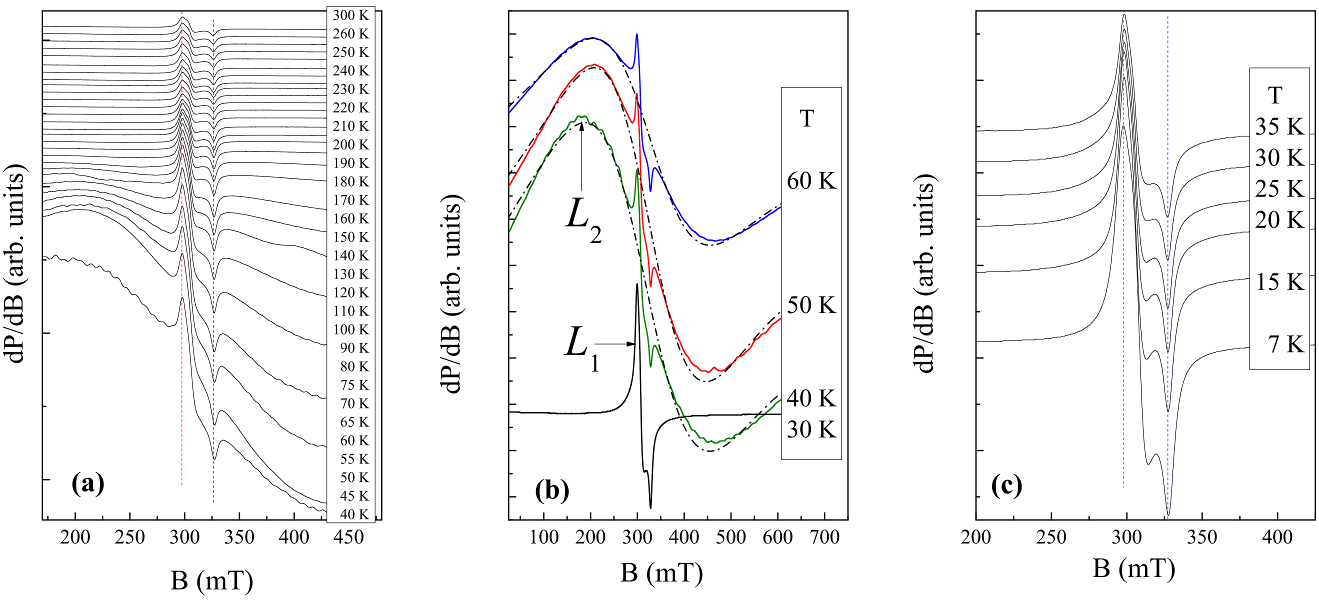

FIG. 11. (Color online) Evolution of ESR spectra of $Cu_3Y(SeO_3)_2O_2Cl$ in the different temperature ranges: (a) Overall high temperature range where the superposition of two modes was observed; (b) the temperature range in the vicinity of Néel temperature (60–30 K) highlighting the disappearance of the L_2 mode below T_N, dash-dotted lines here represent fitting of the L_2 resonance mode by Lorentzian profile; (c) low temperature range showing the behavior of the L_1 mode below T_N. Two resonance modes revealed are denoted by the arrows in (b).

Finally, we turn to a discussion of our ESR study of $Cu_3Y(SeO_3)_2O_2Cl$. The temperature evolution of the powder ESR spectra of $Cu_3Y(SeO_3)_2O_2Cl$ is shown in Fig. 11. Over the whole temperature range studied the ESR powder pattern is characteristic of Cu^{2+} ions with an anisotropic g tensor, while the hyperfine structure expected from natural ^{63}Cu and ^{65}Cu isotopes ($I = 3/2$) is suppressed, presumably due to the presence of weak exchange interactions. The anisotropic line L_1 is superimposed over the extremely wide background line L_2, which is characterized by a comparable resonance field. The line L_2 narrows markedly with decreasing temperature and grows in amplitude [Fig. 11(a)]. The presence of L_2 is most obvious in the temperature range 40–70 K [Fig. 11(b)]. Below 50 K this background line L_2 rapidly broadens and eventually disappears at Néel temperature such that it is no longer detectable at low temperatures [Fig. 11(c)]. The disappearance of the L_2 ESR signal at the Néel temperature is indicative of the opening of a spin gap for the resonance excitation due to the onset of long range magnetic order.

The complex ESR behavior observed here can be understood by taking into account the presence of two different Cu^{2+} sites in the crystal structure of $Cu_3Y(SeO_3)_2O_2Cl$ in addition to the several different exchanges pathways of different energy scales, as outlined in the previous section. The different energy scales of the exchange interaction between the two Cu^{2+} sites are clearly visible from the widths of the ESR branches related to the Cu1 and Cu2. The internal magnetic fields effectively suppress the paramagnetic ESR signal from the Cu2 site at temperatures below $T_N = 36.3$ K, while the signal from the Cu1 remains present even in the low temperature phase. The persistence of the paramagnetic ESR signal below T_N has been observed recently in the mixed dimensionalities system CuP_2O_6 [31] and was explained by the interplay between different exchange couplings in two different magnetic subsystems (1D and 2D) when very weak Cu moments appear within the 1D subsystem of CuP_2O_6. It is worth mentioning that in contrast to the case of $Cu_3Y(SeO_3)_2O_2Cl$, it was not possible to resolve the two different crystallographic Cu^{2+} positions in the ESR spectra of CuP_2O_6.

A detailed quantitative analysis of the ESR line L_2 is complicated due to its extremely large linewidth over almost the whole temperature range studied. Nevertheless, in order to get some quantitative estimations for line L_2 we have fitted the spectra in the temperature range 40–90 K in accordance with a single Lorentzian function of the type

$$\frac{dP}{dB} \propto \frac{d}{dB}\left[\frac{\Delta B}{\Delta B^2 + (B - B_r)^2}\right]$$

where P is the power absorbed in the ESR experiment, B is the applied magnetic field, B_r is the resonance field, and ΔB is the linewidth. Note that during this analysis we have neglected the middle part of the spectrum related to another component L_1. The fitted curves are shown by dash-dotted lines in Fig. 11(b). The effective g factor for line L_2 was found to be about $g = 2.09 \pm 0.02$, while its linewidth exceeds 200 mT at 50 K and markedly increases with increasing temperature.

To evaluate the main ESR parameters of the line L_1 the experimental spectra have been fitted by the sum of the three components corresponding to the principal values of the g tensor. A representative fit of the ESR data is given in Fig. 12(a) with the resolved resonance modes denoted by dashed lines and their sum is shown by the solid line. The temperature dependencies of the effective g factor and linewidth derived from this fitting are shown in Figs. 12(b) and 12(c). The principal g values of the anisotropic g tensor [Fig. 12(b)] remain almost constant over the whole temperature range investigated with average values $g_1 = 2.18(4)$, $g_2 = 2.10(6)$, and $g_3 = 2.05(9)$ resulting in $g = 2.115 \pm 0.005$, which is comparable to both the g values reported for the isostructural compounds $Cu_3Bi(SeO_3)_2O_2Br$ [$g = 2.04(8)$] [16] and $Cu_3Bi(SeO_3)_2O_2Cl$ ($g = 2.16$) [32] and consistent with typical values for Cu^{2+} ions in other copper oxides [33,34]. The slight deviation of the g factors from their high-temperature values below ∼40 K, see Fig. 12(b), is indicative of the development of internal fields upon approaching the long range ordered phase. The observed anisotropy may originate from a sizable spin-orbit coupling λ, which mixes orbital excited states of Cu^{2+} with their Kramer's ground state doublet, and is reflected in measured g-factor shifts of $\Delta g = 0.06$–0.18 from the free electron value of 2.0023. Second-order perturbation theory yields two exchange anisotropy sources, first an antisymmetric Dzyaloshinsky-Moriya (DM) type interaction

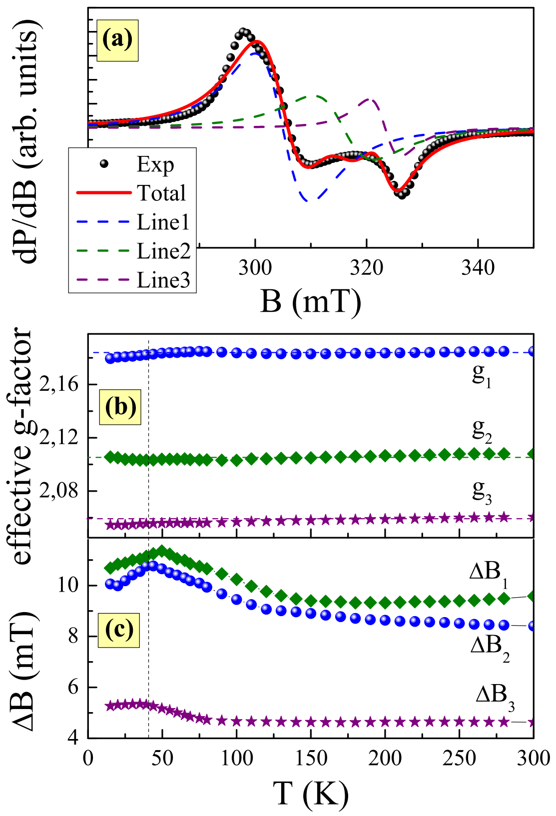

FIG. 12. (Color online) (a) The ESR spectra (circles) of $Cu_3Y(SeO_3)_2O_2Cl$ at 200 K with the fits to the data as described in the text shown by the lines. The dashed lines show the individual Lorentzian fit components and the solid line is the sum of all three. (b) The temperature dependence of principal values of the g tensor. (c) The temperature dependence of the ESR linewidth for three resolved components of the ESR spectra.

$D \propto (\Delta g/g)J$ (linear in λ) and second a symmetric anisotropic exchange (AE) $\mathbf{\Gamma} \propto (\Delta g/g)^2 J$ (quadratic in λ). The DM interaction is usually dominant in Cu-based antiferromagnets, if allowed by symmetry [35].

Several distinct spin dynamic regimes are observed in the temperature dependence of the ESR linewidth [Fig. 12(c)]. The linewidths of all three principal components remain temperature independent at high temperatures ($T > 100$ K), characteristic of the high temperature exchange narrowing regime. Below ∼125 K, conspicuous increases in the linewidths of the ΔB_1 and ΔB_2 components are observed, while ΔB_3 starts to increase noticeably below ∼80 K. Such a broadening is usually taken as evidence for the build-up of short range spin correlations at $T \leqslant J$ [36]. The difference in behavior of ΔB_1 and ΔB_2 in comparison with ΔB_3 indicates that the correlations in $Cu_3Y(SeO_3)_2O_2Cl$ are evolving in an anisotropic manner. Typically ESR spectra tend to broaden monotonically upon lowering temperature as spin correlations develop, which is observed in many other Cu^{2+} based antiferromagnets [37–41]. Nevertheless, the linewidth observed here for $Cu_3Y(SeO_3)_2O_2Cl$ passes through a maximum in the vicinity of Néel temperature and decreases smoothly upon lowering the temperature further, which again may reflect the saturation of the spin correlation length and the depletion of the spin fluctuation density due to the opening of a spin gap [42].

It should be noted that both the large linewidth of the L_2 mode (and, as a consequence, the partial recording of the spectrum within certain temperature ranges) and the anisotropic character of the L_1 mode impede the precise double integration of the derivative absorption curves and leads to noticeable uncertainty in the analysis of the integral ESR intensity, which is proportional to a number of spins. For estimation we have used the conventional relation for the integral intensity $I_{\mathrm{ESR}} \propto A_{\mathrm{ESR}} \Delta B^2$, where A_{ESR} is the amplitude of the ESR signal. Since the experimental spectra of the L_1 mode were treated as a sum of three components corresponding to three principal values of g tensor the total integral ESR intensity can be considered as an average value from those three components. Figure 13 shows this product in comparison with the temperature dependence of the magnetic susceptibility. Apparently the dynamic (ESR) data are in reasonable agreement with static (PPMS) ones. Both data sets show a deviation from the Curie-Weiss law at $T > 120$ K, which is markedly higher than the ordering temperature to be indicative of the strong role of short-range correlations at $T > T_N$ for the present compound. The integral ESR intensity demonstrates the clear tendency to pass through a maximum in the vicinity of Néel temperature but after fracture it begins to increase again with decreasing temperature. One must also take into account that the integral ESR intensity (or resonance magnetic susceptibility χ^{ESR}) cannot be directly related and compared to the static susceptibility because it contains both absorption and dispersion contributions (and static susceptibility is proportional only to the imaginary term of χ^{ESR}). Usually a real part of χ^{ESR} is neglected assuming the dispersion is very low for the dielectric materials. However, for strongly correlated spin systems, especially in the presence of strong short-range correlations, noncollinear spin configuration, frustration, anisotropy, or lower magnetic dimensionality, one may expect an increased role of the dispersion and occurrence of nondiagonal elements of the dynamic susceptibility. So the low temperature increase of I_{ESR1} points to the continuing dynamic processes even in AFM phase similarly to the case of CuP_2O_6 [31] as described above.

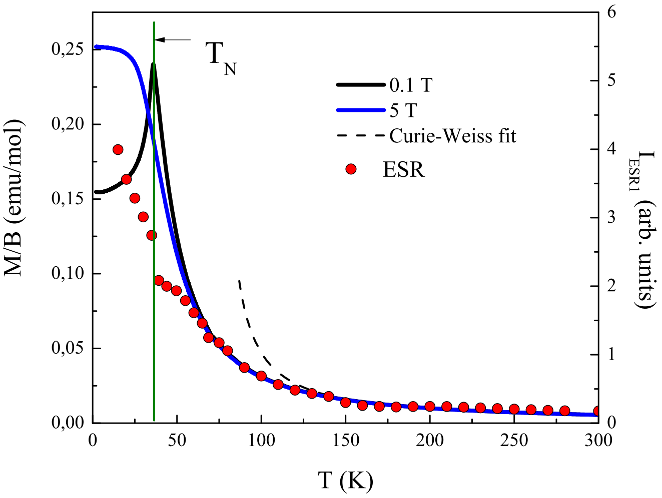

FIG. 13. (Color online) The integral ESR intensity for the L_1 mode (red filled circles) in comparison with static magnetic susceptibility data.

IV. CONCLUSIONS

In conclusion, we have presented a detailed magnetic and first-principles study of the buckled kagome material $Cu_3Y(SeO_3)_2O_2Cl$. $Cu_3Y(SeO_3)_2O_2Cl$ undergoes a magnetic ordering transition at $T_N = 36.3$ K as evidenced by magnetic susceptibility, magnetization, heat capacity, and low temperature neutron diffraction experiments. Rietveld analysis of the low temperature neutron diffraction data revealed that the zero field magnetic structure is described by a canted ferrimagnetic orientation of the Cu^{2+} spins within the buckled kagome layers with an antiferromagnetic stacking between the layers along the c axis. First-principles calculations have allowed for the estimation of both the intraplane and interplane exchange interactions, which are in excellent agreement with our spin model determined from neutron diffraction. The ESR study reveal the presence of two resonance modes corresponding to two different crystallographic Cu positions, which are characterized by almost temperature independent behavior. The principal g values of the g tensor of Cu1 sites were found to be $g_1 = 2.18(4)$, $g_2 = 2.10(6)$, and $g_3 = 2.05(9)$, while the effective g factor of Cu2 sites is almost isotropic and is on average $g = 2.09(5)$. At low temperatures, $Cu_3Y(SeO_3)_2O_2Cl$ undergoes a metamagnetic transition with a critical field $B_C = 2.6$ T at 2 K due to the suppression of the interplane exchange interactions. The relatively weak nature of the interplane coupling results in a low critical field strength while the competition between different intraplane exchange interactions leads to a low saturation field of $B_{\mathrm{sat}} \leqslant 8$ T. Our study suggests that this unusual metamagnetic transition is an inherent property of the francisite family and emphasizes the power one has to extend our understanding of the rich and fascinating physics of this group of materials by simple chemical substitutions.

ACKNOWLEDGMENTS

This work was supported in part from the Ministry of Education and Science of the Russian Federation *in the framework of* Increase Competitiveness Program of NUST "MISiS" (No. K2-2014-036), by the Russian Foundation for Basic Research Projects 12-03-00665, 13-02-00050, 13-02-00174, 13-02-00374, 14-02-00111, 14-02-00245, and 14-02-92002, and by the grants-in-aid of Ministry of Education and Science of Russia MK-3443.2013.2 and MK-7138.2013.2. The collaboration between the University of St Andrews and Moscow State University was funded by a Royal Society International Exchanges grant, in collaboration with the RFBR (12-03-92604). P.L. and L.C. also thank the Leverhulme Trust (Award RPG-2013-343).

---

[1] K. C. Rule, A. U. B. Wolter, S. Suellow, D. A. Tennant, A. Brühl, S. Köhler, B. Wolf, M. Lang, and J. Schreuer, Phys. Rev. Lett. **100**, 117202 (2008).

[2] S. Lebernegg, A. A. Tsirlin, O. Janson, and H. Rosner, Phys. Rev. B **88**, 224406 (2013).

[3] S. Lebernegg, A. A. Tsirlin, O. Janson, and H. Rosner, Phys. Rev. B **87**, 235117 (2013).

[4] M. Schapers, A. U. B. Wolter, S.-L. Drechsler, S. Nishimoto, K.-H. Müller, M. Abdel-Hafiez, W. Schottenhamel, B. Büchner, J. Richter, B. Ouladdiaf, M. Uhlarz, R. Beyer, Y. Skourski, J. Wosnitza, K. C. Rule, H. Ryll, B. Klemke, K. Kiefer, M. Reehuis, B. Willenberg, and S. Süllow, Phys. Rev. B **88**, 184410 (2013).

[5] A. A. Tsirlin, O. Janson, S. Lebernegg, and H. Rosner, Phys. Rev. B **87**, 064404 (2013).

[6] K. Kudo, H. Ishii, M. Takasuga, K. Iba, S. Nakano, J. Kim, A. Fujiwara, and M. Nohara, J. Phys. Soc. Jpn. **82**, 063704 (2013).

[7] S. Kitagawa, H. Kotegawa, H. Tou, H. Ishii, K. Kudo, M. Nohara, and H. Harima, J. Phys. Soc. Jpn. **82**, 113704 (2013).

[8] A. Olariu, P. Mendels, F. Bert, F. Duc, J. C. Trombe, M. A. de Vries, and A. Harrison, Phys. Rev. Lett. **100**, 087202 (2008).

[9] T.-H. Han, S. J. Helton, S. Chu, D. G. Nocera, J. A. Rodrigez-Rivera, C. Broholm, and Y. S. Lee, Nature (London) **492**, 406 (2012).

[10] D. V. Pilon, C. H. Lui, T.-H. Han, D. Shrekenhamer, A. J. Frenzel, W. J. Padilla, Y. S. Lee, and N. Gedik, Phys. Rev. Lett. **111**, 127401 (2013).

[11] D. Wulferding, P. Lemmens, P. Scheib, J. Röder, P. Mendels, S. Chu, T. Han, and Y. S. Lee, Phys. Rev. B **82**, 144412 (2010).

[12] A. Pring, B. M. Gatehouse, and W. D. Birch, Am. Miner. **75**, 1421 (1990).

[13] E. V. Nazarchuk, S. V. Krivovichev, O. Y. Pankratova, and S. K. Filatov, Phys. Chem. Miner. **27**, 440 (2000).

[14] P. Millet, B. Bastide, V. Pashchenko, S. Gnatchenko, V. Gapon, Y. Ksari, and A. Stepanov, J. Mater. Chem. **11**, 1152 (2001); I. Rousochatzakis, J. Richter, R. Zinke, and A. A. Tsirlin, arXiv:1409.4335.

[15] M. Pregelj, O. Zaharko, A. Günther, A. Loidl, V. Tsurkan, and S. Guerrero, Phys. Rev. B **86**, 144409 (2012).

[16] Z. Wang, M. Schmidt, Y. Goncharov, V. Tsurkan, H.-A. Krug von Nidda, A. Loidl, and J. Deisenhofer, Phys. Rev. B **86**, 174411 (2012).

[17] R. Becker and M. Johnsson, Solid State Sci. **7**, 375 (2005).

[18] R. Berrigan and B. M. Gatehouse, Acta Crystallogr. Sect. C **52**, 496 (1996).

[19] P. S. Berdonosov and V. A. Dolgikh, Russ. J. Inorg. Chem. **53**, 1353 (2008).

[20] A. C. Larson and R. B. Von Dreele, Los Alamos National Laboratory Report, No. LAUR-86-748 (1994).

[21] G. A. Bain and J. F. Berry, J. Chem. Ed. **85**, 532 (2008).

[22] M. G. Banks, R. K. Kremer, C. Hoch, A. Simon, B. Ouladdiaf, J.-M. Broto, H. Rakoto, C. Lee, and M.-H. Whangbo, Phys. Rev. B **80**, 024404 (2009).

[23] A. S. Wills, Physica B **276**, 680 (2000), program available from www.ccp14.ac.uk

[24] See Supplemental Material at http://link.aps.org/supplemental/10.1103/PhysRevB.90.214417 for results of the representational analysis of the *Pmmn* structure with the magnetic propogation vector $k = (0,0,0.5)$.

[25] P. Giannozzi *et al.*, J. Phys.: Condens. Matter **21**, 395502 (2009).

[26] J. P. Perdew, K. Burke, and M. Ernzerhof, Phys. Rev. Lett. **77**, 3865 (1996).

[27] S. V. Streltsov and D. I. Khomskii, Phys. Rev. B **86**, 035109 (2012).

[28] S. V. Streltsov, M. V. Petrova, V. A. Morozov, G. V. Romanenko, V. I. Anisimov, and N. N. Lukzen, Phys. Rev. B **87**, 024425 (2013).

[29] W. Geertsma and D. Khomskii, Phys. Rev. B **54**, 3011 (1996).

[30] J. B. Goodenough, *Magnetism and the Chemical Bond* (Interscience, New York, 1963).

[31] R. Nath, K. M. Ranjith, J. Sichelschmidt, M. Baenitz, Y. Skourski, F. Alet, I. Rousochatzakis, and A. A. Tsirlin, Phys. Rev. B **89**, 014407 (2014).

[32] K. H. Miller, P. W. Stephens, C. Martin, E. Constable, R. A. Lewis, H. Berger, G. L. Carr, and D. B. Tanner, Phys. Rev. B **86**, 174104 (2012).

[33] R. M. Krishna and S. K. Gupta, Bull. Magn. Reson. **16**, 239 (1994).

[34] L. Shvanskaya, O. Yakubovich, A. Ivanova, S. Baidya, T. Saha-Dasgupta, E. Zvereva, A. Golovanov, O. Volkova, and A. Vasiliev, New J. Chem. **37**, 2743 (2013).

[35] T. Moriya, Phys. Rev. **120**, 91 (1960).

[36] P. M. Richards, in *Local Properties of Low-Dimensional Antiferromagnets*, edited by K. A. Müller (North Holland, Amsterdam, 1976).

[37] V. Kataev, K.-Y. Choi, M. Grüninger, U. Ammerahl, B. Büchner, A. Freimuth, and A. Revcolevschi, Phys. Rev. Lett. **86**, 2882 (2001).

[38] A. Zorko, D. Arčon, H. van Tol, L. C. Brunel, and H. Kageyama, Phys. Rev. B **69**, 174420 (2004).

[39] Y. C. Arango, E. Vavilova, M. Abdel-Hafiez, O. Janson, A. A. Tsirlin, H. Rosner, S.-L. Drechsler, M. Weil, G. Nénert, R. Klingeler, O. Volkova, A. Vasiliev, V. Kataev, and B. Büchner, Phys. Rev. B **84**, 134430 (2011).

[40] A. Zorko, F. Bert, A. Ozarowski, J. van Tol, D. Boldrin, A. S. Wills, and P. Mendels, Phys. Rev. B **88**, 144419 (2013).

[41] A. U. B. Wolter, F. Lipps, M. Schäpers, S.-L. Drechsler, S. Nishimoto, R. Vogel, V. Kataev, B. Büchner, H. Rosner, M. Schmitt, M. Uhlarz, Y. Skourski, J. Wosnitza, S. Süllow, and K. C. Rule, Phys. Rev. B **85**, 014407 (2012).

[42] F. Chabre, A. M. Ghorayeb, P. Millet, V. A. Pashchenko, and A. Stepanov, Phys. Rev. B **72**, 012415 (2005).